

## Zero-sequence controller requirements and comparison for a delta-CHB STATCOM under unbalanced operation

Iosu Marzo <sup>a,\*</sup>, Ignacio Muguruza <sup>b</sup>, Alain Sanchez-Ruiz <sup>c</sup>, Gonzalo Abad <sup>a</sup>, Hector Fernandez-Rebolleda <sup>b</sup>, Juan José Costa-Iriarte <sup>a</sup>, Jon Andoni Barrena <sup>a</sup>

<sup>a</sup> Electronics and Computer Science Department, Mondragon Unibertsitatea, Loramendi 4, Arrasate-Mondragon, 20500, Spain

<sup>b</sup> Ingeteam Power Technology, Bizkaia Technology Park 110, Zamudio, 48170, Spain

<sup>c</sup> Department of Electronic Technology, University of the Basque Country (UPV/EHU), Nieves Cano 12, Vitoria-Gasteiz, 01006, Spain

### ARTICLE INFO

#### Keywords:

Delta-connected Cascaded H-Bridge (DCHB)  
Intercluster power balancing  
Resonant controller  
Static Synchronous Compensator (STATCOM)  
Unbalanced operation  
Voltage Source Converter (VSC)  
Zero-sequence current

### ABSTRACT

Delta-configured Cascaded H-Bridge (DCHB) topology is a suitable alternative for Static Synchronous Compensator (STATCOM) applications. However, under unbalanced voltage and/or current conditions, zero-sequence current needs to be injected to guarantee dc-link capacitor voltage balancing. The control loop of this zero-sequence current is analyzed in this paper, in order to determine the requirements that the implemented controller must fulfill. Considering these requirements, appropriate transient response and stability margin indicators are defined to quantify and evaluate the performance of different controllers that could be employed—Proportional-Resonant controller (PR), PR controller with delay compensation (PR<sub>d</sub>), and Vector Proportional-Integral controller (VPI) are proposed and analyzed for this application in this paper. Based on the defined indicators, the VPI is the most appropriate among the studied control techniques. Experimental results validate the analytical model of the controllers and their performance.

### 1. Introduction

The Static Synchronous Compensator (STATCOM) using multilevel Voltage Source Converters (VSC) is envisioned as an essential device in both industry and power grid applications. It is used to facilitate the integration of large power consuming loads [1] or renewable energy sources [2], by fulfilling the requirements imposed by power system operators. The typical applications of the STATCOM are the improvement of the power system stability, power factor correction, regulation of line voltages, active power filtering, mitigation of voltage flicker, unbalanced load compensation, and low voltage ride through [3,4].

Besides common advantages of multilevel VSCs [5], those based on modular structures are today the standard for high power – medium voltage applications [6]. As the ac voltage is proportional to the number of power cells, modular structures are scalable, allowing even the transformerless grid connection with improved power quality [1,7]. Foremost among these is the Cascaded H-Bridge (CHB) topology [8], which its use for STATCOM has been receiving considerable attention, in both star (YCHB) and delta (DCHB) configurations.

Requirements from grid codes are changing and have started to demand negative-sequence voltage ( $v^-$ ) and/or current ( $i^-$ ) injection capability from the converters [9]. The unbalanced operation is an issue that the STATCOM must face, in both transmission and distribution

systems. Under unbalanced conditions, the STATCOM should withstand  $v^-$  and/or  $i^-$  [10], or generate them in order to balance the voltage and/or the current at the point of common coupling (PCC) [11].

In this scenario, although there is no net energy exchange between the STATCOM and the power grid, an active power different from zero might appear in each phase of the converter. CHBs present a major drawback under unbalanced conditions: the incapacity to exchange active power among phase clusters due to the lack of a common three-phase dc-link. As a consequence, dc-link voltages may drift away from their reference values [6]. The unbalance of dc-link capacitor voltages causes higher semiconductor stress, can provoke isolation failures, might lead to inject distorted currents into the grid, and even to exceed the operating limits.

The adopted power balancing strategy, also called *intercluster active power balancing*, needs to guarantee an equal active power distribution among phase clusters. In the YCHB it is commonly addressed by adding a zero-sequence voltage, while a zero-sequence current can be added in the case of the DCHB [12–14]. Both solutions have an impact on the power rating of the device, which will limit the capabilities of the STATCOM to provide reactive power [15]. The scientific literature confirms the DCHB as the preferable option for STATCOM application

\* Corresponding author.

E-mail address: [imarzo@mondragon.edu](mailto:imarzo@mondragon.edu) (I. Marzo).

<https://doi.org/10.1016/j.ijepes.2024.109785>

Received 5 December 2022; Received in revised form 13 December 2023; Accepted 9 January 2024

Available online 15 January 2024

0142-0615/© 2024 The Author(s). Published by Elsevier Ltd. This is an open access article under the CC BY-NC-ND license (<http://creativecommons.org/licenses/by-nc-nd/4.0/>).

dealing with unbalanced conditions, since the YCHB is strongly limited by the available dc-side voltage [14–18].

Refs. [12–17,19–29] present different alternatives to perform the intercluster power balancing in the DCHB, which require a controller to track the zero-sequence current ( $i_0^*$ ). Studies [13,14,17,19] have implemented a Proportional controller, and [20–22] a Proportional-Integral (PI) one. Nevertheless, these controllers cause a steady-state error when tracking alternating signals. This might be a major problem in applications where the power converter is required to operate continuously under steady-state conditions with negative sequences, as in traction [30] or industrial arc furnace applications [31,32]. In [15,23–26] a Proportional-Resonant (PR) controller is used. This PR controller guarantees a zero steady-state error [33–35]. However, none of these references analyzes which are the requirements that the controller has to fulfill considering the features of this particular system, nor which control technique is the most adequate.

The main contribution of this paper is to analyze and identify the particularities of the zero-sequence current control loop in a DCHB STATCOM operating with  $v^-$  and/or  $i^-$ , in order to determine the most important requirements to be fulfilled by the implemented controller. Considering these requirements, appropriate transient response and stability margin indicators are defined to quantify and evaluate the performance of the controllers.

Some resonant controllers which are suitable for this loop are compared; apart from the aforementioned PR controller, the PR with delay compensation (PR<sub>d</sub>) [36,37], and the Vector Proportional-Integral (VPI) [38–40] are considered for the comparison. Both could also be suitable to track  $i_0^*$ , but have not been previously proposed for this application. Note that these controllers are not the novelty of this paper, but the definition of the problem in the DCHB STATCOM operating under unbalanced conditions, the mathematical definition of the system with these controllers, as well as the procedure of the comparison are a contribution of this work. An experimental set-up of 100 kVA is also used in order to validate the analytical model of the controllers and their performance.

The paper is outlined as follows. Section 2 presents the DCHB STATCOM and the intercluster power balancing control loop, as well as it describes the most appropriate controllers for that purpose. The explanation of the system particularities, most important requirements, considered evaluation indicators, and the used multi-objective controller parameter selection method is given in Section 3. Section 4 includes the comparison of the controllers. Detailed experimental results are presented in Section 5.

## 2. Delta-connected CHB STATCOM under unbalanced conditions

### 2.1. Topology

Fig. 1 illustrates the layout of a DCHB converter. Each phase cluster consists of  $n$  number of H-bridge power cells, connected in cascade on their ac side. An important characteristic of CHBs is that each power cell is fed by multiple isolated dc energy sources [5,41]. As the phase cluster is rated at the line-to-line voltage, when comparing with the YCHB, either the number of cascaded power cells needs to be increased, or the switching devices have to be sized at higher blocking voltage rating to obtain the same ac voltage in the PCC. However, with the same number of power cells, more current is obtained in the PCC with the delta configuration [6].

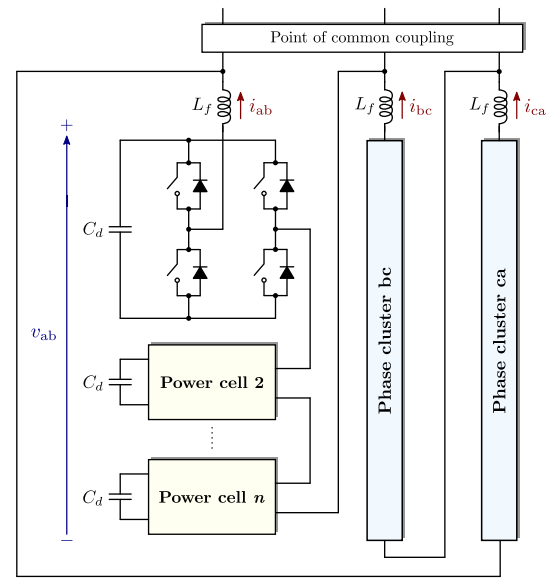


Fig. 1. Simplified circuit diagram of the DCHB converter.

### 2.2. Intercluster active power balancing

The per-phase average active power ( $\bar{P}_{ph}$ ) of the DCHB is calculated by the inner product of the phase cluster voltage and current [6]:

$$\begin{aligned} \bar{P}_{ph} = & \underbrace{\frac{V^+ I^+}{2} \cos(\delta_v^+ - \theta_i^+)}_{\bar{P}_{ph}^{++}} + \underbrace{\frac{V^- I^-}{2} \cos(\delta_v^- - \theta_i^-)}_{\bar{P}_{ph}^{--}} \\ & + \underbrace{\frac{V^+ I^-}{2} \cos(\delta_v^+ - \theta_i^- + k \frac{4\pi}{3})}_{\bar{P}_{ph}^{+-}} \\ & + \underbrace{\frac{V^- I^+}{2} \cos(\delta_v^- - \theta_i^+ - k \frac{4\pi}{3})}_{\bar{P}_{ph}^{-+}} \end{aligned} \quad (1)$$

where  $k = 0, -1, 1$ , for  $ph = ab, bc, ca$ , respectively.  $V^+, V^-, \delta_v^+, \delta_v^-$  denote the converter phase cluster positive- and negative-sequence voltage phasor amplitudes and angles. Likewise,  $I^+, I^-, \theta_i^+, \theta_i^-$  are defined for the current.

The main characteristic of the STATCOM is that there is no need of any energy source, since, neglecting losses, the net active power transfer between the converter and the grid is zero ( $\bar{P}_{ab} + \bar{P}_{bc} + \bar{P}_{ca} = 0$ ). If there is no interaction between positive- and negative-sequence components (only term  $\bar{P}_{ph}^{++}$  or  $\bar{P}_{ph}^{--}$  exists), the average active power which flows into each phase cluster of the STATCOM is also zero; ( $\bar{P}_{ph} = 0$ ). The STATCOM is used in an increasingly wider variety of scenarios in which the operation under  $v^-$  and/or  $i^-$  stands out [9–11]. In this context, terms  $\bar{P}_{ph}^{+-}$  and/or  $\bar{P}_{ph}^{-+}$  appear in (1), which are also different in each phase. This means that phase clusters deliver or absorb an active power different from zero ( $\bar{P}_{ab} \neq \bar{P}_{bc} \neq \bar{P}_{ca} \neq 0$ ).

One disadvantage of CHBs is the lack of a common dc-link, and thereby the difficulty in exchanging active power among phase clusters. Consequently, in order to correct this uneven power distribution and to guarantee dc-link capacitor balancing under unbalanced conditions, countermeasures must be taken [6].

The intercluster power balancing control guarantees that the active power is equally distributed among phase clusters to maintain the charge of the dc-link capacitors. The most widespread alternative in the DCHB is the injection of a fundamental-frequency zero-sequence

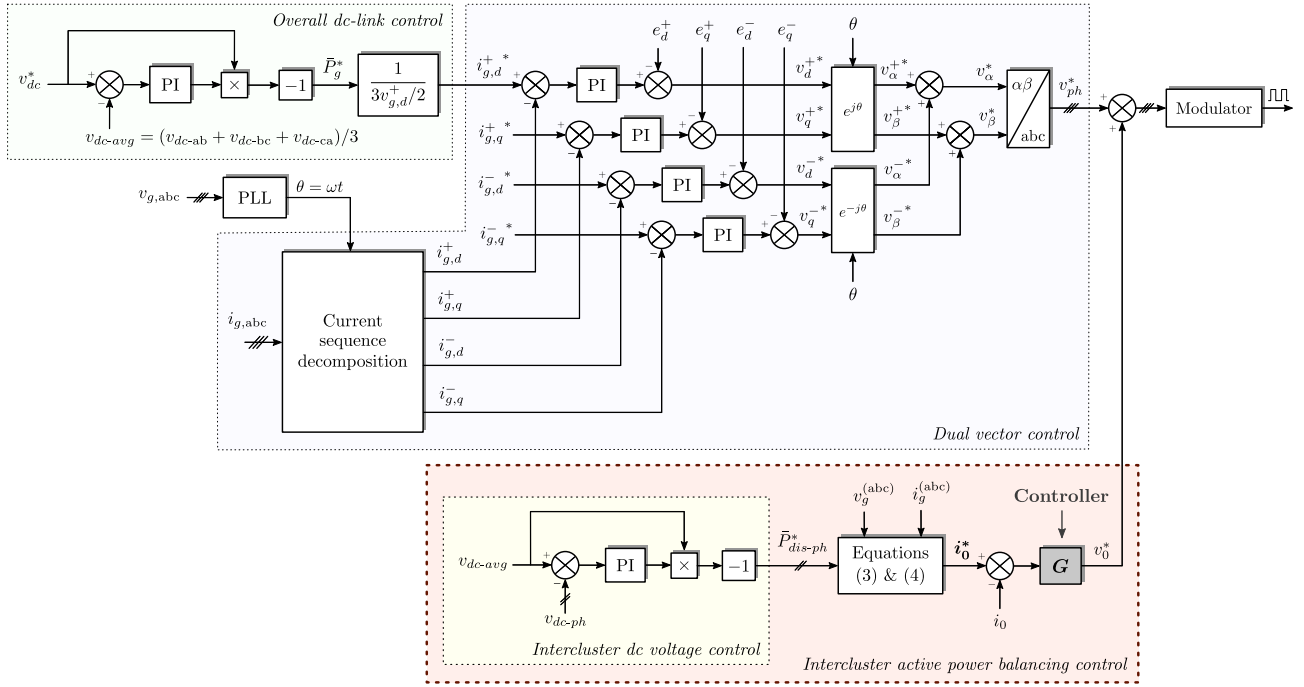


Fig. 2. Simplified block diagram of the overall control design of the DCHB STATCOM to operate with  $v^-$  and/or  $i^-$ .

current ( $i_0$ ) [12–15]:

$$i_0(t) = I_0 \sin(\omega t + \theta_{i_0}) \quad (2)$$

Since it circulates only inside the delta, the added  $i_0$  does not affect the grid-side three-phase voltages and currents. The aim is to find an appropriate amplitude ( $I_0$ ) and angle ( $\theta_{i_0}$ ), which will cancel out the effect of the non-zero average active power at each phase cluster due to the cross-interaction between positive- and negative-sequences ( $\bar{P}_{ph}^{+-}$  and/or  $\bar{P}_{ph}^{-+}$ ), as well as it will compensate for any type of power disturbance caused by non-idealities ( $\bar{P}_{dis}$ ), preserving the dc-link voltages in each phase cluster adjusted to the reference value ( $K$  constant terms are defined in Appendix) [12–15]:

$$\tan \theta_{i_0} = \frac{(\bar{P}_{dis-bc} - K_1^{bc})K_2^{ab} - (\bar{P}_{dis-ab} - K_1^{ab})K_2^{bc}}{(\bar{P}_{dis-ab} - K_1^{ab})K_3^{bc} - (\bar{P}_{dis-bc} - K_1^{bc})K_3^{ab}} \quad (3)$$

$$I_0 = \frac{\bar{P}_{dis-ph} - K_1^{ph}}{K_2^{ph} \cos \theta_{i_0} + K_3^{ph} \sin \theta_{i_0}} \quad (4)$$

### 2.3. Overall control design

The control of the DCHB STATCOM under unbalanced conditions requires addressing both the overall dc-link voltage unbalance and the intercluster active power unbalance (see Fig. 2). This is composed of three main parts: the dual vector control, the overall dc-link voltage control, and the intercluster active power balancing control.

Three-phase grid currents ( $i_{g,abc}$ ) are decomposed into positive- and negative-sequences, and are transformed to the  $dq$ -reference frame using the transformation angle ( $\theta = \omega t$ ) provided by the Phase-Locked Loop (PLL), which synchronizes the converter with the positive-sequence grid voltage ( $v_g^+$ ). The positive- and negative-sequence  $dq$  components of the measured current are estimated using the Delayed Signal Cancellation (DSC) technique [42], and the dual vector control allows to control both sequences independently [43] (tuned as [44]). The obtained converter reference voltages are then transformed to three-phase quantities ( $v_{ab}^*$ ,  $v_{bc}^*$ ,  $v_{ca}^*$ ), and the converter switching pattern is obtained by the modulator.

The overall dc-link voltage controller is required to absorb the sufficient three-phase active power from the power grid ( $\bar{P}_g^*$ ) to compensate

for power losses and non-idealities across the converter. It generates the necessary  $d$ -component positive-sequence current ( $i_d^{+*}$ ) for maintaining the average dc-link voltage adjusted at the reference value ( $v_{dc}^*$ ).

The equality of the three-phase dc-link voltages is guaranteed by the intercluster active power balancing control. The required  $i_0^*$  is calculated from (3) and (4), according to the power disturbances in each phase cluster ( $\bar{P}_{dis-ph}^*$ ) generated by the intercluster dc voltage control. In order to redistribute the active power equally among phase clusters, a zero-sequence voltage ( $v_0^*$ ) needs to be generated, which is then added to the dual vector control output voltage references ( $v_{ab}^*$ ,  $v_{bc}^*$ ,  $v_{ca}^*$ ), and will lead to the calculated reference of  $i_0^*$  [14].

### 2.4. Controllers for the zero-sequence current loop

Several studies have used the zero-sequence current injection in the DCHB STATCOM to operate with  $v^-$  and/or  $i^-$  [12–17,19–29]. Some of these have used a Proportional controller as  $G$  in Fig. 2 to track the fundamental-frequency reference  $i_0^*$  [13,14,17,19], while in [20–22] a Proportional-Integral (PI) control is used. However, based on classical control theories [45], the closed-loop frequency response of a PI regulator shows that it is not possible to guarantee a zero steady-state error when controlling alternating signals; and neither with a Proportional controller. In other words, there will be an unavoidable steady-state error in both the calculated amplitude  $I_0^*$  and the phase  $\theta_{i_0}^*$ . The impossibility to track properly  $i_0^*$  might make that the active power will not be redistributed equally among phase clusters, and it might lead to dc-link capacitor voltage drifting, resulting in not synthesizing correctly the output voltage. Studies [15,23–26] have added a Proportional-Resonant (PR) controller, which is a better alternative than the previous ones since it is capable of tracking  $i_0^*$  with a zero steady-state error. This can be seen in the examples in Figs. 3 and 4, where simulations of a 5-level Neutral Point Clamped H-Bridge (5L NPC/HB) converter are shown in the event of a voltage unbalance at  $t = 800$  ms. However, none of the mentioned sources [13–15,17,19–26] analyzes the requirements that the controller has to fulfill considering the features of this particular system, nor which control technique is the most appropriate.

Although the PI is one of the most established control techniques in many applications, its utilization to track sinusoidal signals is limited.

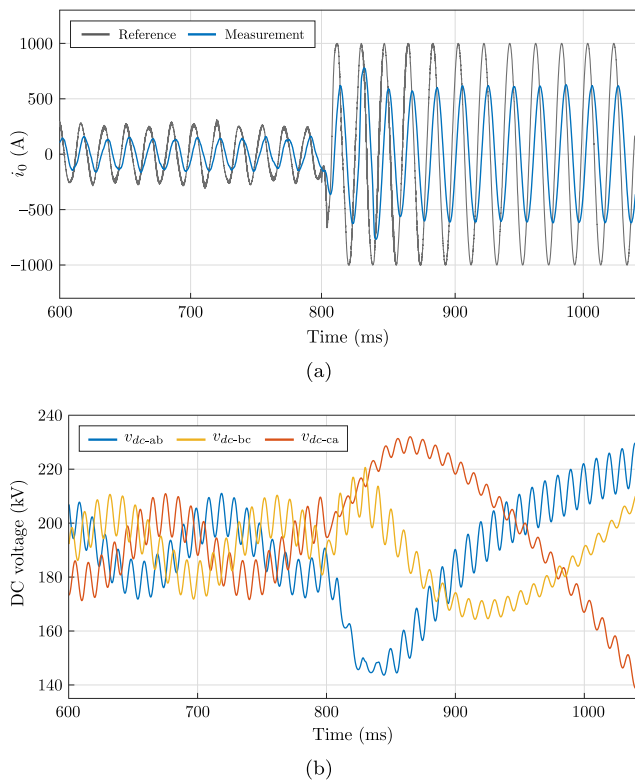


Fig. 3. Intercluster active power balancing using a Proportional controller. (a)  $i_0$  reference and measurement, and (b) DC-link voltage in each phase cluster.

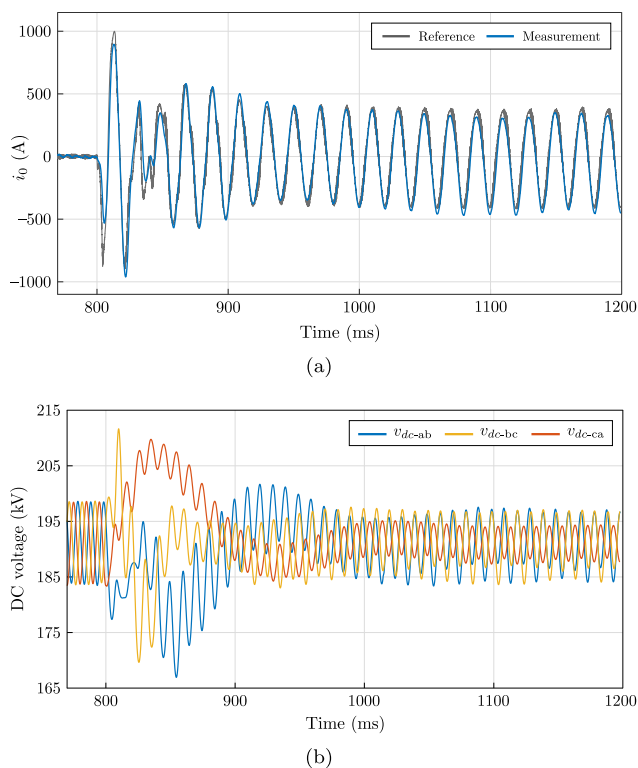


Fig. 4. Intercluster active power balancing using a PR controller. (a)  $i_0$  reference and measurement, and (b) DC-link voltage in each phase cluster.

PI controllers in stationary frame involve a considerable steady-state error, since they only guarantee a perfect tracking of the reference at

0 Hz [40]. Note that by implementing two independent PI controllers separately at the same time, one for the amplitude  $I_0^*$  and one for the angle  $\theta_0^*$ , the reference  $i_0^*$  could be controlled with zero steady-state error. A resonant controller is equivalent to the latter, with an important saving of computational burden due to the reduction in the number of regulators [33–35]. Although the PR is the only resonant controller that has been used in the literature for the  $i_0$  control loop in a DCHB [15,23–26], other controllers of this family such as the PR with delay compensation (PR<sub>d</sub>), and the Vector Proportional-Integral (VPI) are analyzed and compared in this paper, which could be suitable for the system under study.

#### 2.4.1. PR controller

The  $s$ -domain transfer function of a PR controller can be expressed as [34,35]

$$G_{PR}(s) = K_p + \frac{K_i s}{s^2 + \omega_0^2} \quad (5)$$

being  $K_p$  and  $K_i$  the proportional and integral gains, and  $\omega_0$  the resonant angular frequency.  $G_{PR}(s)$  provides infinite gain in open-loop at the resonant frequency ( $f_0$ ), and thus unity gain and zero phase shift in closed-loop; ensuring zero steady-state error when tracking any signal pulsating at  $\omega_0$  [40].

#### 2.4.2. PR controller with delay compensation

In real systems, the computation or the implemented modulation scheme generate a delay which affects the system performance and might cause instability. Therefore, a delay compensation can be added to the PR controller in (5), whose resulting transfer function in the  $s$  domain can be expressed as [36]

$$G_{PR_d}(s) = K_p + \frac{K_i (s \cos(\phi) - \omega_0 \sin(\phi))}{s^2 + \omega_0^2} \quad (6)$$

where  $\phi$  is the phase lead introduced in the vicinity of  $\omega_0$ ; i.e., the difference between the actual phase provided by the real controller at frequencies infinitely close to  $f_0$  and that provided by  $G_{PR}(s)$ . In order to compensate for  $n_d$  number of sampling periods,  $\phi = n_d \omega_0 T_s$  should be applied, being  $T_s$  the sampling period. Normally,  $n_d = 1.5-2$  is often considered [37], depending on the modulation technique used. The delay compensation becomes more crucial as  $\omega_0$  increases with respect to the sampling angular frequency ( $\omega_s$ ) [40]; e.g., in MV power converters which operate at low  $f_s$ .

#### 2.4.3. VPI controller

When employing resonant controllers, undesired peaks might appear around  $f_0$  in closed-loop, mainly because of the terms of the plant not compensated by  $G_{PR}(s)$ . This bad performance is aggravated when the frequency ( $f$ ) deviates from its expected value ( $f_0$ ) [40]. Lascu et al. proposed an alternative resonant regulator to PR ones, known as Vector Proportional-Integral (VPI) controller [38,39]:

$$G_{VPI}(s) = \frac{K_p s^2}{s^2 + \omega_0^2} + \frac{K_i s}{s^2 + \omega_0^2} \quad (7)$$

The aim of this regulator is the cancellation of the pole of any plant with the form of  $G_{PI}(s) = 1/(L_f s + R_f)$ , being  $L_f$  and  $R_f$  the inductance and its resistive value. Note that this is the form of the plant of the zero-sequence current control loop under study. The plant pole cancellation is achieved by maintaining the relationship  $K_i/K_p = R_f/L_f$ , obtaining

$$G_{VPI}(s) = \frac{K_h s(L_f s + R_f)}{s^2 + \omega_0^2} \quad (8)$$

where  $K_h = K_p/L_f$ . By doing so, and neglecting the effects of the computational delay or the modulation, the plant pole is canceled

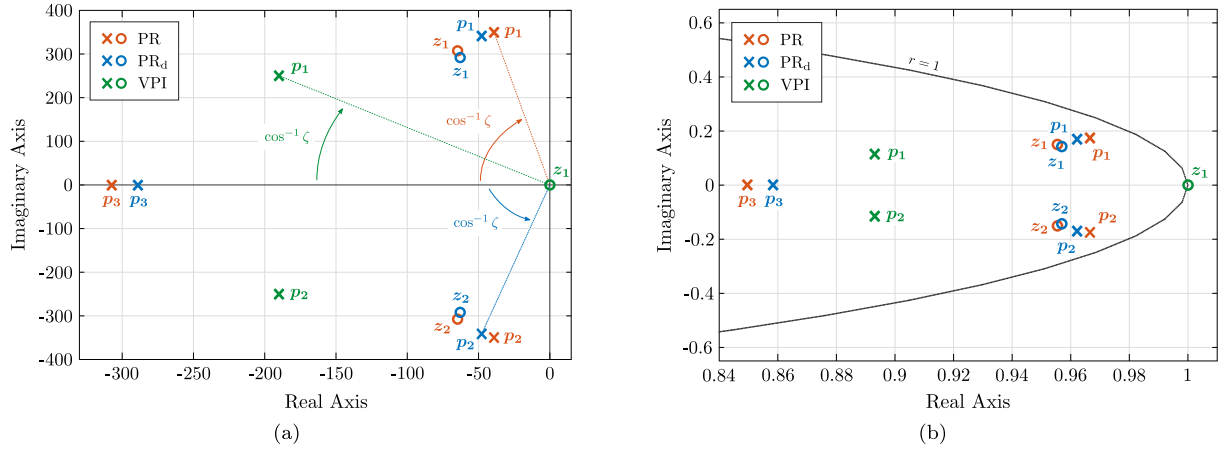


Fig. 5. Closed-loop pole-zero map of each controller tuned at  $\omega_0 = 50$  Hz. (a)  $s$ -domain, and (b)  $z$ -domain with ZOH technique.  $K_p$  and  $K_i$  are 0.95 and 123 for the PR and  $PR_d$ , and 0.95 and 5.7 for the VPI.  $L_f$  and  $R_f$  of the plant are 2.5 mH and 15 m $\Omega$ , respectively, while  $T_s$  is 500  $\mu$ s.

**Table 1**  
Closed-loop  $s$ -domain transfer functions of each controller.

Controller	$C_L(s) = (G(s)G_{PL}(s))/(1 + G(s)G_{PL}(s))$
<b>PR</b>	$\frac{K_p s^2 + K_i s + K_p \omega_0^2}{L_f s^3 + (R_f + K_p)s^2 + (L_f \omega_0^2 + K_i)s + (R_f + K_p)\omega_0^2}$
<b><math>PR_d</math></b>	$\frac{K_p s^2 + K_i s \cos \phi + K_p \omega_0^2 - K_i \omega_0 \sin \phi}{L_f s^3 + (R_f + K_p)s^2 + (L_f \omega_0^2 + K_i \cos \phi)s + (R_f + K_p)\omega_0^2 - K_i \omega_0 \sin \phi}$
<b>VPI</b>	$\frac{K_p s^2 + K_i s}{L_f s^3 + (R_f + K_p)s^2 + (L_f \omega_0^2 + K_i)s + R_f \omega_0^2} \xrightarrow{K_i/K_p=R_f/L_f} \frac{K_h s}{s^2 + K_h s + \omega_0^2}$

**Table 2**  
Numerator coefficients of the  $z$ -domain transfer functions of the resonant controllers using the ZOH method.

	<b>PR</b>	<b><math>PR_d</math></b>	<b>VPI</b>
$a_0$	$K_p$	$K_p$	$K_p$
$a_1$	$\frac{K_i}{\omega_0} \sin(\omega_0 T_s) - 2K_p \cos(\omega_0 T_s)$	$\frac{K_i}{\omega_0} (\sin(\omega_0 T_s) + \phi) - 2K_p \cos(\omega_0 T_s)$	$\frac{K_i}{\omega_0} \sin(\omega_0 T_s) - K_p (\cos(\omega_0 T_s) + 1)$
$a_2$	$K_p - \frac{K_i}{\omega_0} \sin(\omega_0 T_s)$	$K_p - \frac{K_i}{\omega_0} (\sin(\omega_0 T_s) + \phi) + \sin \phi$	$K_p \cos(\omega_0 T_s) - \frac{K_i}{\omega_0} \sin(\omega_0 T_s)$

by one of the zeros of the VPI regulator, resulting in the following simplified open-loop transfer function [40]:

$$G_{VPI}(s)G_{PL}(s) = \frac{K_h s}{s^2 + \omega_0^2} \quad (9)$$

In practice, due to system non-idealities and the effect of the temperature, the estimation of the plant ( $L_f$  and  $R_f$ ) is not straightforward. As a consequence, and accompanied with unavoidable calculation errors, the plant pole cancellation is complicated in practical applications. However, it has been proven that the non-cancellation of the plant pole have little influence on the stability margins, transient response, and parameter tuning of the VPI controller [39,46]. Besides, the fact that the zero-sequence plant is not as variable as the grid-equivalent makes the VPI an interesting alternative, which its utilization has not been proposed for the system under study.

Fig. 5(a) shows the closed-loop  $s$ -domain pole-zero map of each resonant controller and a LR plant  $G_{PL}(s)$ , whose transfer functions are shown in Table 1. Both the PR and  $PR_d$  have a complex conjugate pole pair  $p_1-p_2$ , a complex conjugate zero pair  $z_1-z_2$ , and a real pole  $p_3$ . For its part, the plant pole cancellation causes the VPI to have one pole and one zero less. As can be seen, the complex conjugate pole pair of the VPI has greater damping ratio ( $\zeta \uparrow$ ) than the PR and  $PR_d$  ones, which makes the VPI have a much damper and less oscillating response than common regulators. Regarding the  $PR_d$ , Fig. 5(a) shows that the position of the poles and zeros is similar with respect to the PR when tracking fundamental-frequency signals.

Both  $G_{PR_d}(s)$  and  $G_{VPI}(s)$  permit to reduce anomalous peaks in the closed-loop frequency response with respect to  $G_{PR}(s)$ , providing higher stability margins [40]. An important advantage of  $G_{VPI}(s)$  is that it offers more damped response than  $G_{PR}(s)$  and  $G_{PR_d}(s)$  [47,48]. Besides,  $G_{VPI}(s)$  only requires the delay compensation for very high-order harmonics [39], being in these cases  $G_{PR_d}(s)$  a preferable option [46].

Any controller expressed in the  $s$  domain has to be discretized to the  $z$  domain to be implemented in digital devices. Due to their selectivity and hence the dependence on the accuracy at  $\omega_0$  [40], resonant controllers are especially sensitive to the discretization process. Inaccuracies such as displacement of poles, or influence on the delay compensation effectivity, might result in significant loss of performance, especially for tracking high frequency signals; the non-infinite gain at the expected frequency does not assure zero steady-state error, and might compromise stability. That is the reason why the VPI is often optimized by a combination of the most adequate discrete-time implementations for each resonant term in (7). Nevertheless, it has been proven that the discretization method has no influence when tracking fundamental-frequency (such as  $i_0^*$ ) and low-order harmonic references. Consequently, although it is not the most popular method in digital controller design since it has many drawbacks [46], for simplicity and for the comparison to be fair, the regulators have been discretized with the same method: Zero-Order Hold (ZOH). The controllers under study share the  $z$ -domain transfer function in (10), each of them having different coefficients in the numerator, collected in Table 2.

$$G(z) = \frac{a_0 + a_1 z^{-1} + a_2 z^{-2}}{1 - 2z^{-1} \cos(\omega_0 T_s) + z^{-2}} \quad (10)$$

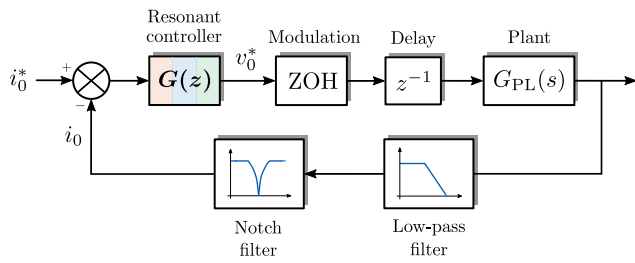


Fig. 6. Block diagram of the  $i_0$  control loop.

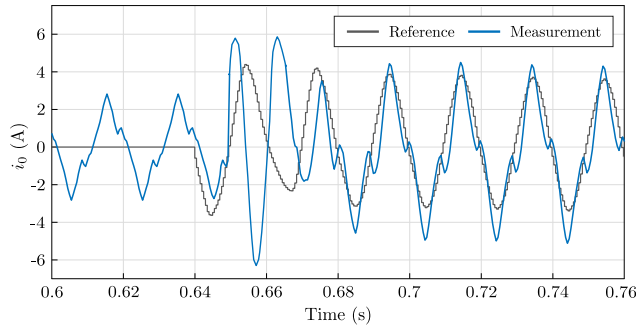


Fig. 7. Presence of the  $3\omega$  component in the simulated zero-sequence current measurement due to the introduced  $7.5 \mu s$  dead times.

Fig. 5(b) also shows the closed-loop  $z$ -domain pole-zero map of each resonant controller and the plant  $G_{PL}(z)$ , using the ZOH method and a  $500 \mu s$  sampling period.

### 3. System requirements

#### 3.1. System description

The  $z$ -domain closed-loop diagram of this particular system is shown in Fig. 6, which is based on the experimental set-up of Section 5. The system analytical model is composed of the following blocks:

- $G(z)$  represents the discrete-domain resonant controller (either PR, PR<sub>d</sub> or VPI), which tracks the reference  $i_0^*$ , tuned at  $\omega_0 = \omega$ .
- A ZOH block models the used Space Vector Modulation (SVM).
- $z^{-1}$  models the one sample computational delay.
- The zero-sequence LR plant inside the delta clusters. Its  $s$ -domain transfer function is derived as follows:

$$3v_0(t) = 3L_f \frac{di_0(t)}{dt} + 3R_f i_0(t)$$

$$v_0 = L_f i_0 s + R_f i_0 \quad (11)$$

$$G_{PL}(s) = \frac{i_0}{v_0} = \frac{1}{L_f s + R_f}$$

By discretizing the plant also with the ZOH method, the effect of the used SVM is already considered; i.e., a half of a sample delay [40,49]. It should be noted that the zero-sequence circuit is formed by the path inside the delta connection. For certain current and/or voltage unbalance at the converter terminals, the  $i_0$  loop under study is independent of the grid-side filter.

- The measured three-phase currents are filtered by a first-order low-pass filter, being  $\omega_c$  the cut-off frequency:

$$H_{lpf}(s) = \frac{1}{s + \omega_c} \quad (12)$$

- In order to guarantee that both upper and lower switches in the power cell leg never conduct simultaneously, dead times are introduced, especially in high power converters such as the one

Table 3  
System requirements and corresponding indicators.

Requirement	Indicator
Speed of response	Settling time ( $t_{set}$ )
$3\omega$ attenuation	Gain of $D_L(z)$ at $3\omega$
Overshoot minimization	0-crossing overshoot Peak-crossing overshoot
Robustness to $L_f$ and $R_f$ uncertainty	Sensitivity

in this study. These dead times might generate a zero-sequence third-order harmonic ( $3\omega$ ) component [50–52], which can circulate within the delta-connected clusters. As a consequence, the  $3\omega$  component will appear in the zero-sequence current measurement added to the fundamental one. Fig. 7 shows the simulated zero-sequence current measurement in the experimental set-up of Section 5 with  $7.5 \mu s$  dead times introduced, in which the weight of  $3\omega$  can be clearly appreciated. In order to prevent this component from being coupled with the controller response (so that does not affect the assumed active power distribution in the calculation of  $i_0^*$ ), the system must be able to attenuate it. The specialized literature makes no mention about this problem in DCHB STATCOMs, but the authors have experimentally verified that this  $3\omega$  component might generate instabilities in the control loop. Thus, the authors recommend adding a notch filter tuned at  $\omega_n = 3\omega$  to the measured zero-sequence current (see Fig. 6). The  $s$ -domain transfer function of the notch filter can be expressed as

$$H_{notch}(s) = \frac{s^2 + \omega_n^2}{s^2 + 2\zeta\omega_n s + \omega_n^2} \quad (13)$$

being  $\omega_n$  the notch frequency, and  $\zeta$  the damping ratio.

#### 3.2. Requirements and indicators

Considering the particularities of the closed-loop system model of Fig. 6, the aim is to identify the most important requirements to be fulfilled by the implemented controller. These requirements are quantified and evaluated by means of some indicators, which are obtained through the system time response, frequency response Bode diagrams, and  $z$ -domain pole-zero map analysis. Then, controllers will be compared based on these indicators. Table 3 lists each system requirement and its corresponding evaluation indicator.

##### 3.2.1. Speed of response

Converter inner loops like the one under study have to be fast enough for the outer loops to be effective. This system requires the controller to be fast so that the dc-link voltages do not drift away from their reference value. The indicator used to measure the system speed of response is the settling time ( $t_{set}$ ), which corresponds to the time needed to reach the final value of the reference. The position of the poles and zeros determines the transient response of the system.  $t_{set}$  is determined by the pole with the biggest module in the  $z$  domain, not having a zero nearby that tends to cancel its effect; this is called dominant pole. The dominant pole presents the smallest decay rate ( $\lambda$ ) at the time-domain response, being  $A$  the residue and  $Ae^{-\lambda t}$  the exponentially decaying component corresponding to that pole. Its time constant ( $\tau$ ) is determined by the pole location as

$$\tau = \frac{1}{\lambda} = \frac{-T_s}{\ln r} \quad (14)$$

where  $r$  is the module of the dominant pole, and  $t_{set}$  corresponds to  $3\tau$ . Thus, dominant poles will be the ones whose effect needs more time to be extinguished during transients (slowly decaying components); i.e., the bigger the module of the dominant pole ( $r \uparrow$ ), the slower the system ( $t_{set} \uparrow$ ). The transient response can be optimized by making poles

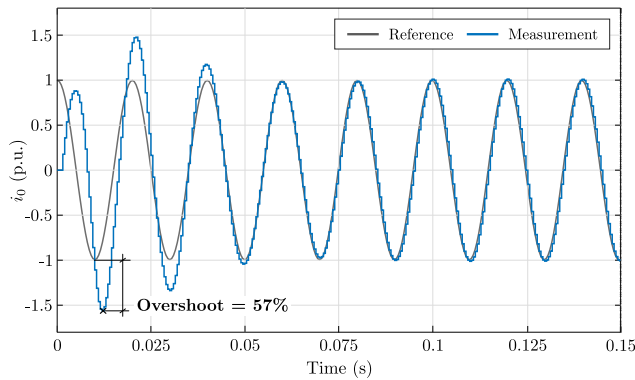


Fig. 8. Reference peak-crossing overshoot calculation.

fast ( $\lambda \uparrow$  and  $r \downarrow$ ), and by placing them next to zeros that cancel their effect ( $A \downarrow$ ) [47].

Dominant poles are also the ones that are closer to the instability limit circle ( $r = 1$  in the  $z$ -domain pole-zero). Therefore, by setting the dominant poles within a desired module (keeping  $r < 1$  to guarantee the stability), in addition to defining  $t_{set}$ , the stability margin is also determined [44]. The dominant pole corresponds to the closed-loop

$$C_L(z) = \frac{G(z) z^{-1} G_{PL}(z)}{1 + D_L(z)} \quad (15)$$

being the direct-loop the following:

$$D_L(z) = G(z) z^{-1} G_{PL}(z) H_{lpf}(z) H_{notch}(z) \quad (16)$$

Note that, in this system, when selecting  $t_{set}$  of the controller  $G$ , the bandwidth of the outer loops of the converter (e.g., the overall dc-link control) needs to be properly selected.

### 3.2.2. Third-order harmonic attenuation

As mentioned, the zero-sequence control loop under study is vulnerable to the  $3\omega$  component in the zero-sequence current measurement, especially in high power applications. The added  $z$ -domain notch filter will attenuate this component, but it will not eliminate it completely, so one of the main requirements of the resonant controller is to mitigate it as much as possible. The indicator to quantify this requirement is the gain at  $3\omega$  of the system direct-loop  $D_L(z)$  frequency response.

### 3.2.3. Overshoot minimization

High  $i_0$  overshoot values could lead the current exceeding the rated level of semiconductor devices. The overshoot for an alternating signal input depends also on the phase of the reference at the instant when the transient occurs [53], being the zero-crossing of  $i_0^*$  the most favorable case (min. overshoot), and the peak-crossing the most unfavorable (max. overshoot). Both cases are distinguished, which are obtained calculating the system time response maximum amplitude with respect to the reference amplitude, as the example in Fig. 8 shows.

### 3.2.4. Robustness to plant parameters uncertainty

It is important for a system to remain stable even if the parameters of the plant vary. This paper proposes the use of a single indicator to evaluate the stability margin (robustness) of the system in the face of the uncertainty of  $L_f$  and  $R_f$  [44,54]. The uncertainty refers to the deviation of this parameters with respect to the nominal values used to design the controller. The indicator to measure the robustness proposed by the authors is the sensitivity, which quantifies the percentage of the closed-loop systems with unstable poles ( $r > 1$ ) obtained for a certain deviation of the plant parameters (see example of Fig. 9). For the calculation of the sensitivity, a deviation of  $\pm 20\%$  with an increment of 2% has been considered for  $L_f$ , and  $-50\%$  to  $+100\%$  with an increment of 10% for  $R_f$  (see Table 4). A sweep of all these values (338 systems in total) allows quantifying how many of these are unstable systems.

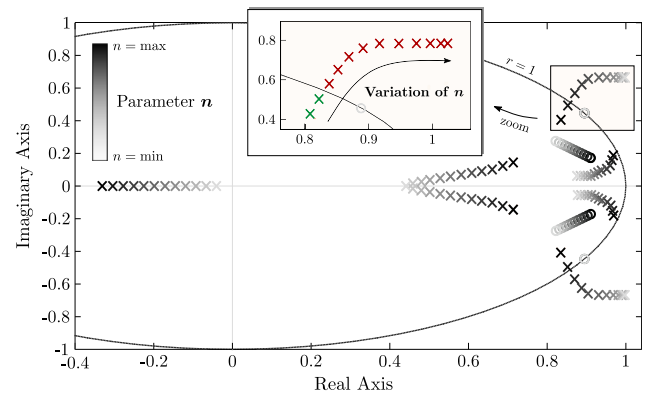


Fig. 9. Graphical example of the sensitivity to become unstable due to poles displacement in the face of the variation of the parameter  $n$ . In this example, where 10  $L_f$ - $R_f$  pairs are unstable (red poles) and 2 stable (green poles), the sensitivity is  $10/12 = 83.3\%$ .

Table 4

Parameters of the system under study.

Parameter	Value
Sampling period ( $T_s$ )	500 $\mu$ s
Fundamental and resonant frequency ( $f_0 = f$ )	50 Hz
Inductive filter ( $L_f$ )	2.5 mH
Deviation	$\pm 20\%$
Resistance ( $R_f$ )	15 m $\Omega$
Deviation	$-50\%/+100\%$
Filter cut-off frequency ( $f_c$ )	1 kHz
Notch frequency ( $f_n = 3f$ )	150 Hz
Notch damping ( $\zeta$ )	$1/4\pi$
Dominant pole max. time constant ( $\tau$ )	3.5 s
Compensated sampling periods in the PR <sub>d</sub> ( $n_d$ )	1.5
Normalization of the indicators	
Settling time ( $t_{set}$ )	$3\tau_f = 500$ ms
$3\omega$ amplification	0.2 p.u.
Overshoot (0- and peak-crossing)	50%
Sensitivity	50%

### 3.3. Indicator normalization

In order to compare controllers, the calculated indicators should be normalized. The base values are chosen considering the elements and characteristics of the system; in this case, the experimental set-up used in Section 5 to validate the theoretical study. The proposed criteria for calculating the base values are the following:

- $t_{set}$  is normalized to three times the time constant of the plant ( $3\tau_f = 3L_f/R_f$ ).
- The base value of the amplification of the  $3\omega$  component is set to 0.2 p.u. This value has been chosen empirically because the authors have experimentally verified that above this value this system might present stability problems.
- Assuming the capacity to withstand transitory overloads in an air-cooled VSC, both 0- and peak-crossing overshoot values are normalized to 50%. This value can be increased with water-cooled power converters.
- The values of the sensitivity are normalized to 50%.

Considering these criteria, the base values used in this paper are collected in Table 4.

### 3.4. Multi-objective controller parameter selection

In this paper, the tuning of the controllers is carried out based on the defined indicators. To choose a suitable combination of the parameters  $K_p$  and  $K_i$  in each controller, as a first step, the stability of the system

**Table 5**

$K_p$  and  $K_i$  parameters for each tuning criteria of the resonant controllers in the system under study.

	(a) Balanced	(b) $t_{set} \downarrow$	(c) $3\omega$ amp. $\downarrow$	(d) 0-crossing ov. $\downarrow$	(e) Peak-crossing ov. $\downarrow$	(f) Sens. $\downarrow$
<b>PR</b>	$K_p = 0.95$ $K_i = 124$	$K_p = 1.35$ $K_i = 252$	$K_p = 0.5$ $K_i = 19$	$K_p = 1.35$ $K_i = 32$	$K_p = 1.05$ $K_i = 21$	$K_p = 1.4$ $K_i = 322$
<b>PR<sub>d</sub></b>	$K_p = 0.95$ $K_i = 122$	$K_p = 1.25$ $K_i = 223$	$K_p = 0.35$ $K_i = 36$	$K_p = 1.2$ $K_i = 11$	$K_p = 0.95$ $K_i = 29$	$K_p = 1$ $K_i = 321$
<b>VPI</b>	$K_p = 0.45$ $K_i = 2.7$	$K_p = 1$ $K_i = 6$	$K_p = 0.05$ $K_i = 0.3$	$K_p = 0.65$ $K_i = 3.9$	$K_p = 0.05$ $K_i = 0.3$	$K_p = 1.4$ $K_i = 8.4$

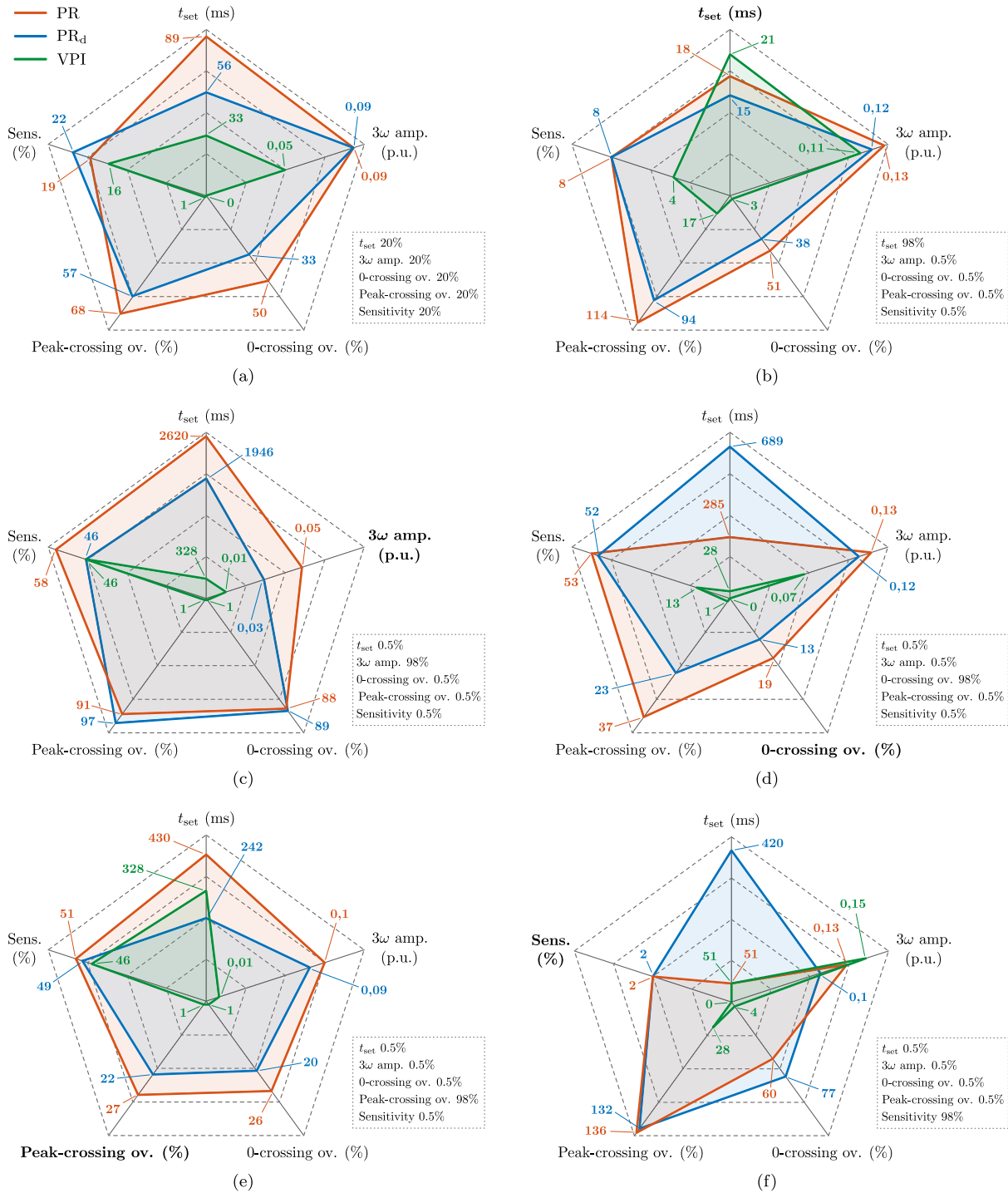


**Fig. 10.** Comparison spider charts of the PR, PR<sub>d</sub> and VPI controllers for different tuning criteria. (a) Balanced tuning, which gives the same priority to minimize all the indicators, (b) prioritizing a fast transient response ( $t_{set} \downarrow$ ), (c) prioritizing the attenuation of the  $3\omega$  component (amplification  $\downarrow$ ), (d) prioritizing the input 0-crossing overshoot minimization, (e) prioritizing the input peak-crossing overshoot minimization, and (f) prioritizing the robustness of the system in the face of the uncertainty of  $L_f$  and  $R_f$  (sensitivity  $\downarrow$ ).

is analyzed in order to identify the range of values in which the system is stable. Within this valid range of values, a sweep of  $K_p$  and  $K_i$  is performed, and the normalized values of the defined indicators are calculated at each point.

The proposed multi-objective controller parameter selection method is based on giving a weight to each indicator, and finds a certain combination of  $K_p$  and  $K_i$  depending on the criteria used to fulfill the requirements of the system. That is, the values of  $K_p$  and  $K_i$  which obtain the minimum of the sum of all indicators with the corresponding weighting.

#### 4. Controller comparison

An important feature of MV STATCOMs is that they operate at relatively low switching frequencies (1 kHz), where the  $\omega_s/\omega_0$  ratio is not so large. However, as the ratio  $\omega_s/\omega_0$  increases,  $G_{PR_d}(s)$  and  $G_{VPI}(s)$  present more advantages over  $G_{PR}(s)$  [40]. Therefore, it is essential to quantify the extent to which they improve the system under study. This approach is particularly reasonable given the lack of studies comparing these controllers.

The comparison between PR,  $PR_d$  and VPI controllers in the system under study is presented by means of spider charts in Fig. 10. In these, the values of the indicators of each controller are shown for six different tuning criteria. First, controllers are compared in the so-called “balanced tuning”, where the same priority (weighting) is given to all the indicators; i.e., a weight of 20% for each indicator. The other five tuning criteria prioritize the minimization of one indicator; e.g., aim a fast transient response ( $t_{set} \downarrow$ ), or a great stability margin (sensitivity  $\downarrow$ ). In this case, the highest weighting is given to the target indicator: 98%, and 0.5% to the other four indicators.

As the aim is to minimize the indicators, the controller with the smallest area is the most suitable. Note that each spider chart should be analyzed separately, since the scaling of the axes is different in each of them. Table 5 collects the  $K_p$  and  $K_i$  corresponding to each tuning criteria. It can be seen that in the VPI the relationship between  $K_i$  and  $K_p$  is always the same in order to guarantee the plant pole cancellation ( $K_i/K_p = R_f/L_f = 6$ ). Table 4 shows the values of the parameters of the system in which the comparison is made, assuming the elements and characteristics of the experimental set-up used in Section 5 to validate the theoretical study.

The results show that giving almost all the weight to one indicator can be prejudicial to other indicators. The most appropriate performance is therefore obtained with the balanced tuning in Fig. 10(a) (first column in Table 5). It can be seen how the VPI obtains the lowest values in each of the indicators.

The time response of the balanced tuning of each regulator for a reference zero-crossing input is presented in Fig. 11(a). The fastest transient response (lowest  $t_{set}$ ) corresponds to the VPI, followed by the  $PR_d$ , and the PR. This can also be deduced in the pole-zero map of the balanced tuning in Fig. 11(b), where the dominant pole pair  $p_3-p_4$  of the VPI has the smallest module ( $r$ ), and the dominant pole pair  $p_1-p_2$  of the PR the biggest, the latter having therefore the slowest time response (biggest  $t_{set}$ ). Note that the complex pole pair  $p_1-p_2$  belongs to the original poles of each controller, shown in Fig. 5(a) and (b).

In terms of the overshoot, Fig. 11(a) shows that the PR has the highest value, somewhat greater than the  $PR_d$ , for both reference zero- and peak-crossing inputs. It should be emphasized that the VPI has practically no overshoot, regardless of how it is tuned. This characteristic of the VPI can be explained by the position of the poles in Fig. 5. The overshoot of a system depends on the damping ratio ( $\zeta$ ) of its complex conjugate pole pairs, which are responsible of the oscillatory component in the time-domain response (a decaying sinusoidal); greater  $\zeta$ , less overshoot. From Fig. 5(a), the high  $\zeta$  of the original pole pair  $p_1-p_2$  results in the VPI having no overshoot; that is, the decaying sinusoidal component corresponding to this pole pair has hardly any oscillation. For its part, the original pole pairs  $p_1-p_2$  of the PR and  $PR_d$  have a

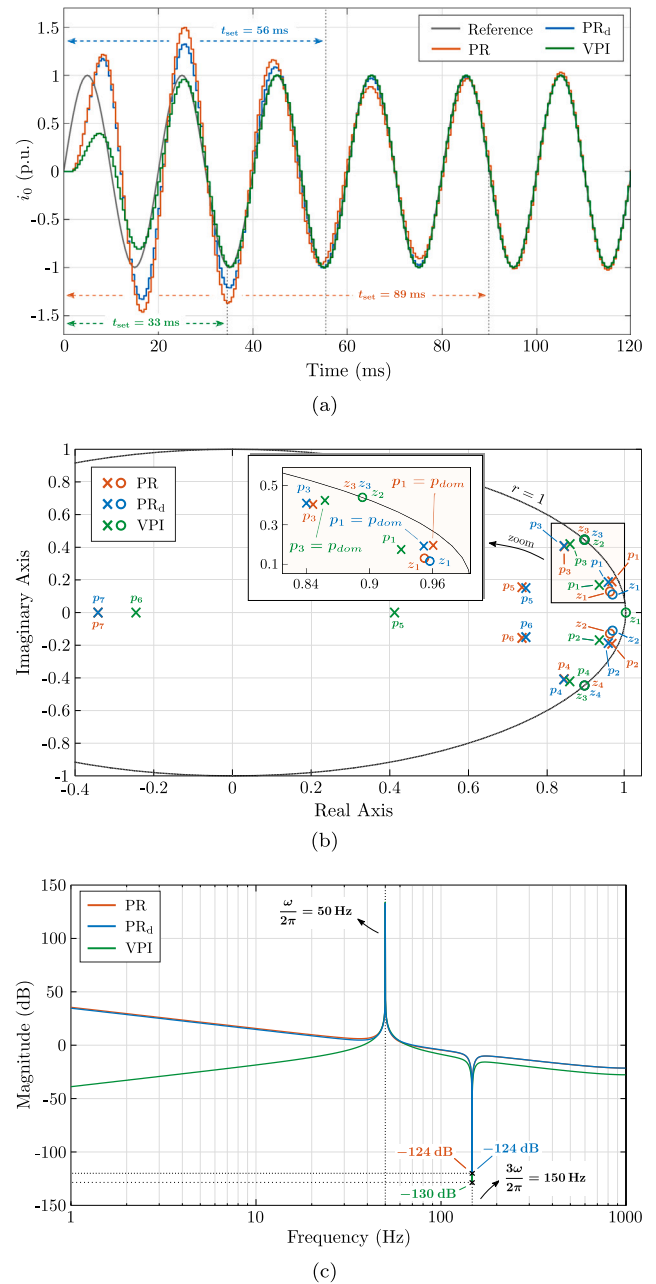


Fig. 11. Balanced tuning of the PR,  $PR_d$  and VPI controllers in Fig. 10(a). (a) Time response with reference zero-crossing input, (b) closed-loop ( $C_L$ ) z-domain pole-zero map, and (c) direct-loop ( $D_L$ ) z-domain Bode diagram.

very low damping ( $\zeta \ll 1$ ), which causes the PR and  $PR_d$  to have high overshoot, being that their major disadvantage.

Regarding the attenuation of the  $3\omega$  component, it is calculated by the direct-loop  $D_L(z)$  Bode diagram, shown in Fig. 11(c) for the balanced tuning case of Fig. 10(a). As this frequency response shows, the three systems offer a very high gain at the  $\omega_0$  to which they have been tuned ( $\omega_0$ ), and very low gain around the notch frequency ( $\omega_n$ ). The system based on the VPI has the lowest gain at  $3\omega$ , and thus the smallest amplification of this harmonic component. The gain at any frequency in  $D_L(z)$  of any of the three systems is proportional to the parameter  $K_p$ ; so the lower  $K_p$ , the higher the attenuation at  $3\omega$ , as Table 5 confirms. The VPI is also the most robust controller in the face of the uncertainty of  $L_f$  and  $R_f$  in the balanced tuning, as well as in the rest of the tuning criteria.

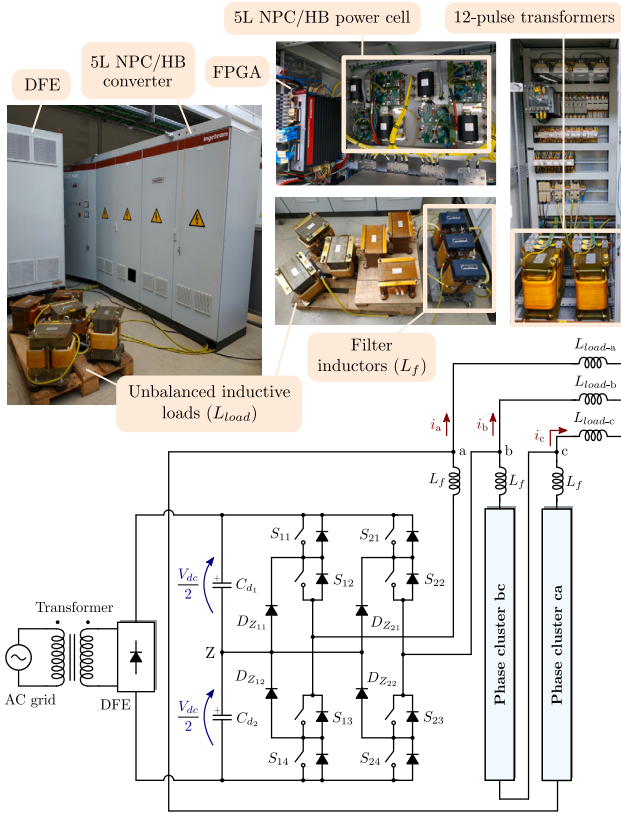


Fig. 12. Experimental set-up layout and circuit diagram.

Table 6  
Experimental set-up parameters.

Parameter	Value
Rated power ( $S_r$ )	100 kVA
Rated voltage ( $V_{ll-rms}$ )	500 V
Power cell dc-link voltage ( $V_{dc}$ )	430 V
Power cell dc-link capacitor ( $C_d = C_{d_1}/2 = C_{d_2}/2$ )	0.825 mF
Switching frequency	1 kHz
Intercluster dc voltage control PI tuning	
Proportional gain ( $K'_p$ )	0.006
Integral gain ( $K'_i$ )	0.02

To sum up, the VPI controller is the preferable option to the PR and  $PR_d$  for the system under study, due to its fast time response, robustness,  $3\omega$  attenuation, and, above all, almost no overshoot. Besides, note that the improvement obtained with the  $PR_d$  with respect to the PR is not noticeable for this fundamental-frequency  $i_0$  control loop.

### 5. Experimental results

Experimental results obtained from a 500 V – 100 kVA 5L NPC/HB converter are provided to validate the system analytical model and the performance of the controllers studied in this paper for the  $i_0$  loop in the DCHB STATCOM when operating with  $i^-$ . The layout of the experimental set-up built in the Medium Voltage Laboratory of Ingeteam Power Technology S.A. (Zamudio, Spain), and its simplified circuit diagram are shown in Fig. 12. The parameters of the set-up and the experiments are given in Table 6.

By an open-loop scalar voltage/frequency regulation, the 5L NPC/HB converter synthesizes positive-sequence voltage ( $v^+$ ), and connected to single-phase unbalanced inductive loads ( $L_{load-ph}$ ) to emulate a STATCOM scenario without net energy exchange (other than power losses),  $i^-$  circulation is generated through the converter. For these

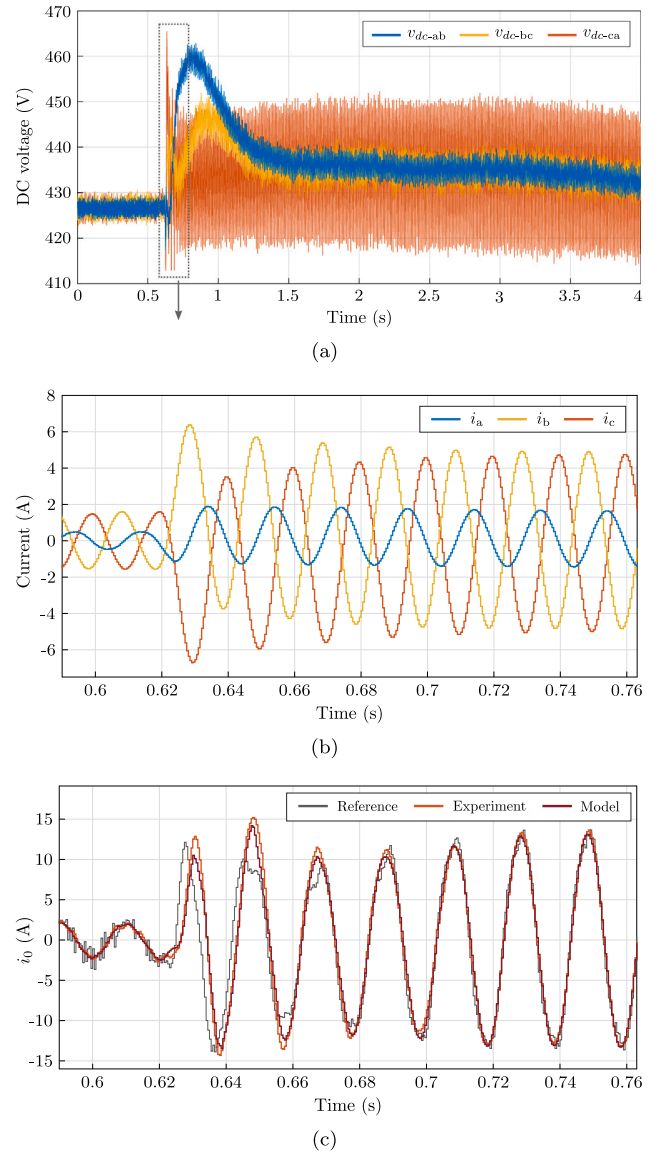


Fig. 13. PR with reference 0-crossing change in its balanced tuning.  $V_{ll-rms}$  is increased from 50 V to 150 V.  $L_{load-a} = L_{load-b} = 3.2$  mH, and  $L_{load-c} = 18.2$  mH. (a) DC-link voltage in each phase cluster, (b) load currents, and (c)  $i_0$  reference, measurement and analytical model.

tests, 3.2 mH and 7.5 mH loads are combined to generate different unbalanced current scenarios, which will request the injection of  $i_0$ . Each phase cluster is composed of a single 5L NPC/HB power cell ( $n = 1$ ), with the aim of avoiding the intracluster unbalance and isolating the analyzed intercluster balancing control. Single-phase inductances of 2.5 mH are used as a filter inside the delta ( $L_f$ ); which form the plant of the zero-sequence loop with its resistive value ( $R_f = 15$  m $\Omega$ ). The switching scheme used is the multilevel SVM with a switching frequency of 1 kHz.

Since the VSC is not connected to the grid, and is feeding passive loads, it is necessary to have an energy source connected to the dc-links. That is why these experiments are performed using a 12-pulse Diode Front End (DFE) rectifier connected to each power cell. For the results that this paper aims to validate, these experiments are valid. If the intercluster active power balancing strategy does not regulate properly, dc-link capacitor voltages will remain unbalanced, and even some of the dc-link voltages could continuously increase above the dc

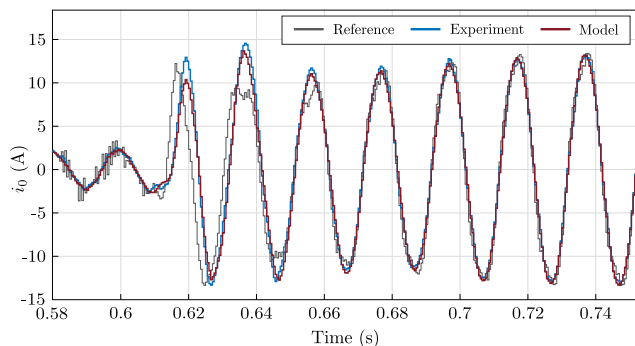


Fig. 14.  $i_0$  reference, measurement and analytical model of the PR<sub>d</sub> with reference 0-crossing change in its balanced tuning.  $V_{ll-rms}$  is increased from 50 V to 150 V.  $L_{load-a} = L_{load-b} = 3.2$  mH, and  $L_{load-c} = 18.2$  mH.

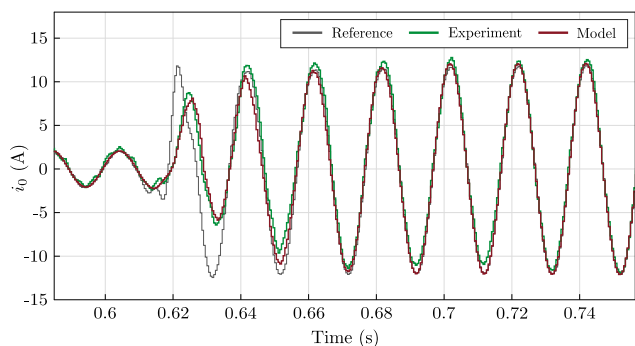


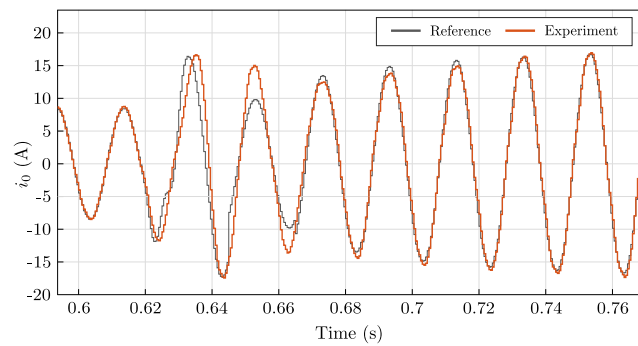
Fig. 15.  $i_0$  reference, measurement and analytical model of the VPI with reference 0-crossing change in its balanced tuning.  $V_{ll-rms}$  is increased from 50 V to 150 V.  $L_{load-a} = L_{load-b} = 3.2$  mH, and  $L_{load-c} = 18.2$  mH.

voltage set by the DFE rectifier. Therefore, the overall dc-link control of Fig. 2 is not needed for these experiments.

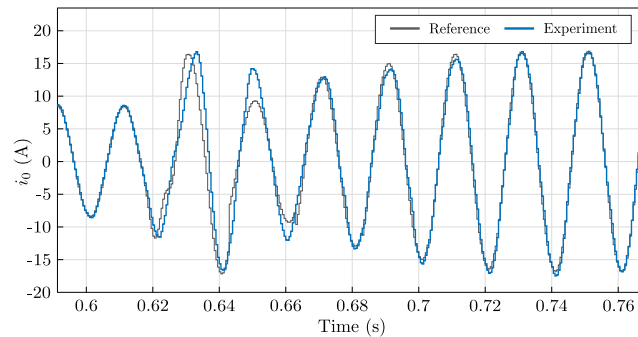
In order to validate the theoretical analysis, a step change of the voltage reference ( $V_{ll-rms}$ ) modifies the reference  $i_0^*$  to be injected according (3) and (4); this will allow to analyze and compare the transient response of each controller studied. Firstly, the analytical model of the system (i.e., the system z-domain transfer function) is validated with the measured  $i_0$  in the experimental set-up for the PR, PR<sub>d</sub> and VPI. For that purpose, the PI of the intercluster dc voltage control in Fig. 2 has been tuned in the same way for all the tests so that it does not affect the conclusions (see Table 6).

In the first tests,  $L_{load-a}$  and  $L_{load-b}$  are 3.2 mH, while  $L_{load-c}$  is 18.2 mH; i.e.,  $I^-/I^+ = 0.55$ . Fig. 13(a) shows the dc-link voltages in each phase cluster ( $v_{dc-ab}, v_{dc-bc}, v_{dc-ca}$ ), which begin to drift away when  $i_0^*$  is modified by means of increasing  $V_{ll-rms}$  from 50 V to 150 V. Without the DFE, at least one of the dc capacitors would discharge. The voltage reference is changed at a particular phase so that  $i_0^*$  changes at its zero-crossing. It can be seen how the intercluster power balancing control adjusts the dc-link voltages in each phase cluster to the reference value. Since  $i_0$  circulates only inside the DCHB, its injection does not affect the output unbalanced load currents ( $i_a, i_b, i_c$ ), which are shown in Fig. 13(b). The resonant controller used in this test is the PR, and Fig. 13(c) shows the  $i_0$  reference, the corresponding response of the analytical model, and the test measurement. The balanced tuning of Fig. 10(a) and the first column of Table 5 is used in this experiment. Figs. 14 and 15 show the transient response of the same experiment using the PR<sub>d</sub> and the VPI, respectively.

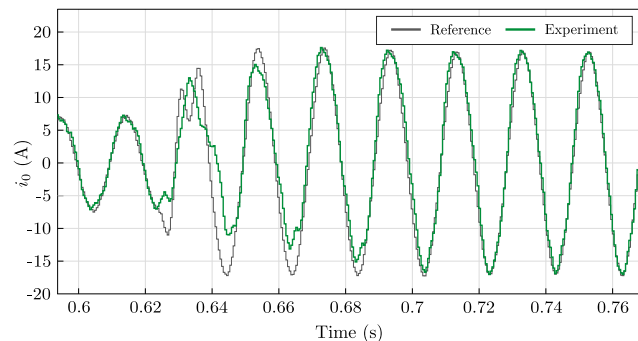
The experiments in Figs. 13–15 show that the analytical model response and the  $i_0$  measurement match well, which completely validates the analytical model (see Fig. 6), as well as the conclusions of the comparison. Regarding the performance of the controllers, it is difficult



(a)



(b)



(c)

Fig. 16.  $i_0$  reference and measurement with reference peak-crossing change in the balanced tuning.  $V_{ll-rms}$  is increased from 100 V to 200 V.  $L_{load-a} = L_{load-b} = 3.2$  mH, and  $L_{load-c} = 18.2$  mH. (a) PR, (b) PR<sub>d</sub>, and (c) VPI.

to evaluate the  $t_{set}$  of the transient response of each one, and it is even more difficult considering that  $i_0^*$  is different in each experiment; it depends on the other control loops of the converter, and varies until the three dc-link voltages are equalized. However, it can be seen how the three systems respond relatively fast. What is noteworthy is the overshoot, which is almost null with the VPI compared to the PR and PR<sub>d</sub>, where the overshoots are about 40–50%; values close to those obtained in Fig. 10(a).

Once the analytical model has been validated, the following figures show two other test scenarios, tuned also with the balanced tuning, but with a reference peak-crossing disturbance. On the one hand, in Fig. 16 the voltage reference  $V_{ll-rms}$  change is modified, where it goes from 100 V to 200 V. On the other hand, a different current unbalance is generated in the experiments of Fig. 17;  $L_{load-a}$  is 3.2 mH, while  $L_{load-b}$  and  $L_{load-c}$  are 10.7 mH ( $I^-/I^+ = 0.27$ ).  $V_{ll-rms}$  goes from 100 V to 250 V in this case. Both tests confirm the advantage of the VPI over the PR and PR<sub>d</sub>: more damped response with no overshoot. Besides, in these experiments it can be seen how the VPI is faster as it reaches the final value earlier. As for the PR<sub>d</sub>, it can be said that its behavior and

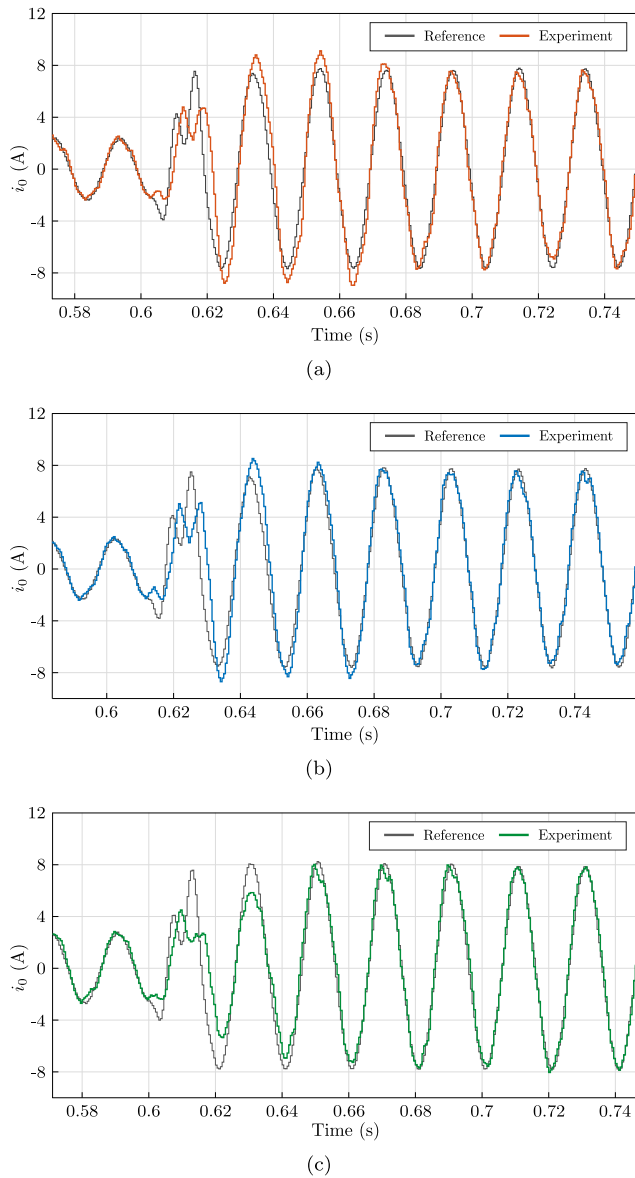


Fig. 17.  $i_0$  reference and measurement with reference peak-crossing change in the balanced tuning.  $V_{ll-rms}$  is increased from 100 V to 250 V.  $L_{load-a} = 3.2$  mH, and  $L_{load-b} = L_{load-c} = 10.7$  mH. (a) PR, (b) PR<sub>d</sub>, and (c) VPI.

dynamic response are not advantageous in this application since they are very similar to the PR. It can be seen how the achieved results meet the theoretical approach.

## 6. Conclusion

The DCHB converter is a suitable alternative for STATCOM applications operating with  $v^-$  and/or  $i^-$ . However, a zero-sequence current ( $i_0$ ) needs to be injected in this situation to redistribute equally the active power among phase clusters and to guarantee dc-link capacitor voltage balancing. This paper has identified the particularities of this  $i_0$  control loop, with the aim of determining the requirements to be fulfilled by the implemented controller.

It should be noted that in high power applications such as the one in this study, the addition of the proposed notch filter attenuates the  $3\omega$  component in the measured  $i_0$ , thus solving a serious problem caused by dead times, which could affect very negatively the assumed intercluster active power redistribution.

Based on the identified requirements, appropriate indicators have been defined to quantify and evaluate the performance of some controllers which are suitable for this loop —PR, PR<sub>d</sub> and VPI are proposed in this paper. The used multi-objective controller parameter selection method have allowed to tune the controllers using different criteria which prioritize the defined indicators, and a comparison of the controllers has been presented.

The carried out comparison confirms the VPI as the preferable option to the PR and PR<sub>d</sub> due to its fast time response, robustness,  $3\omega$  attenuation, and especially, no overshoot. The VPI, with very few exceptions, improves all the indicators of the other two controllers with the six tuning criteria analyzed. Regarding the need of a delay compensation, the improvements of the PR<sub>d</sub> with respect to the PR are not appreciable in this scenario where a fundamental-frequency signal needs to be tracked. The comparison presented has been supported by experimental results which completely validate the analytical model of the three resonant controllers and their performance. The experimental analysis also validates that the defined indicators are valid to quantify the behavior of the controllers for the system under study.

## CRedit authorship contribution statement

**Iosu Marzo:** Conceptualization, Methodology, Software, Validation, Visualization, Writing – original draft. **Ignacio Muguruza:** Conceptualization, Methodology, Software, Validation, Writing – review & editing. **Alain Sanchez-Ruiz:** Conceptualization, Methodology, Supervision, Validation, Writing – review & editing. **Gonzalo Abad:** Conceptualization, Methodology, Supervision, Writing – review & editing. **Hector Fernandez-Rebolleda:** Validation. **Juan José Costa-Iriarte:** Software. **Jon Andoni Barrena:** Conceptualization, Methodology, Supervision, Writing – review & editing.

## Declaration of competing interest

The authors declare that they have no known competing financial interests or personal relationships that could have appeared to influence the work reported in this paper.

## Data availability

No data was used for the research described in the article.

## Acknowledgments

This work was supported in part by the Ministry of Education and Vocational Training of Spain under Grant FPU18/04246, and in part by the Ministry of Industry, Trade and Tourism of Spain through the Project “Grid Ancillary Services Autonomous Converter (GASAC)” under Grant RTC-2017-26091-3.

## Appendix. Terms for the calculation of $i_0$

$$\begin{aligned}
 K_1^{ph} &= V^+ I^- \cos\left(\delta_v^+ - \theta_i^- + k \frac{4\pi}{3}\right) \\
 &\quad + V^- I^+ \cos\left(\delta_v^- - \theta_i^+ - k \frac{4\pi}{3}\right) \\
 K_4^{ph} &= V^+ \cos\left(\delta_v^+ + k \frac{2\pi}{3}\right) + V^- \cos\left(\delta_v^- - k \frac{2\pi}{3}\right) \\
 K_5^{ph} &= V^+ \sin\left(\delta_v^+ + k \frac{2\pi}{3}\right) + V^- \sin\left(\delta_v^- - k \frac{2\pi}{3}\right) \\
 K_6^{ph} &= I^+ \cos\left(\theta_i^+ + k \frac{2\pi}{3}\right) + I^- \cos\left(\theta_i^- - k \frac{2\pi}{3}\right) \\
 K_7^{ph} &= I^+ \sin\left(\theta_i^+ + k \frac{2\pi}{3}\right) + I^- \sin\left(\theta_i^- - k \frac{2\pi}{3}\right) \\
 K_2^{ph} &= K_4^{ph} + X_f K_7^{ph} \quad K_3^{ph} = K_5^{ph} + X_f K_6^{ph}
 \end{aligned} \tag{A.1}$$

## References

- [1] Akagi H. Classification, terminology, and application of the modular multilevel cascade converter (MMCC). *IEEE Trans Power Electron* 2011;26(11):3119–30.
- [2] Carrasco JM, Franquelo LG, Bialasiewicz JT, Galván E, Guisado RCP, Martín Prats MÁ, Leon JI, Moreno-Alfonso N. Power-electronic systems for the grid integration of renewable energy sources: a survey. *IEEE Trans Ind Electron* 2006;53(4):1002–16.
- [3] Balıkcı A, Akpınar E. A multilevel converter with reduced number of switches in STATCOM for load balancing. *Electr Power Syst Res* 2015;123:164–73.
- [4] Duarte SN, Ghetti FT, de Almeida PM, Barbosa PG. Zero-sequence voltage compensation of a distribution network through a four-wire modular multilevel static synchronous compensator. *Int J Electr Power Energy Syst* 2019;109:57–72.
- [5] Kouro S, Malinowski M, Gopakumar K, Pou J, Franquelo LG, Wu B, Rodriguez J, Pérez MA, Leon JI. Recent advances and industrial applications of multilevel converters. *IEEE Trans Ind Electron* 2010;57(8):2553–80.
- [6] Marzo I, Sanchez-Ruiz A, Barrena JA, Abad G, Muguza I. Power balancing in cascaded H-bridge and modular multilevel converters under unbalanced operation: A review. *IEEE Access* 2021;9:110525–43.
- [7] Hu P, Guerrero JM, He Z. Design and analysis of a transformerless STATCOM based on hybrid cascaded multilevel converter. *Int J Electr Power Energy Syst* 2019;104:694–704.
- [8] Peng FZ, Lai J-S, McKeever JW, VanCoeveering J. A multilevel voltage-source inverter with separate DC sources for static VAR generation. *IEEE Trans Ind Appl* 1996;32(5):1130–8.
- [9] Tanaka T, Ma K, Wang H, Blaabjerg F. Asymmetrical reactive power capability of modular multilevel cascade converter based STATCOMs for offshore wind farm. *IEEE Trans Power Electron* 2019;34(6):5147–64.
- [10] IEC 61000-2-4. Electromagnetic compatibility (EMC) – Part 2-4: Environment - Compatibility levels in industrial plants for low-frequency conducted disturbances. 2004.
- [11] Verband der Elektrotechnik Elektronik Informationstechnik (VDE). Technical connection rules for high-voltage (VDE-AR-N 4120). 2018.
- [12] Betz RE, Summers T, Furney T. Symmetry compensation using a H-bridge multilevel STATCOM with zero sequence injection. In: 41st IAS annu. meet. conf. rec. 2006 ind. appl. conf.. 2006, p. 1724–31.
- [13] Hagiwara M, Maeda R, Akagi H. Negative-sequence reactive-power control by a PWM STATCOM based on a modular multilevel cascade converter (MMCC-SDBC). *IEEE Trans Ind Appl* 2012;48(2):720–9.
- [14] Behrouzian E, Bongiorno M. Investigation of negative-sequence injection capability of cascaded H-bridge converters in star and delta configuration. *IEEE Trans Power Electron* 2017;32(2):1675–83.
- [15] Marzo I, Barrena JA, Sanchez-Ruiz A, Abad G, Fernandez-Rebolledo H, Muguza I. Reactive power limits of cascaded H-bridge STATCOMs in star and delta configuration under negative-sequence current withstanding. *Int J Electr Power Energy Syst* 2022;142:108267.
- [16] Oghorada OJK, Zhang L. Analysis of star and delta connected modular multilevel cascaded converter-based STATCOM for load unbalanced compensation. *Int J Electr Power Energy Syst* 2018;95:341–52.
- [17] Oghorada OJK, Zhang L. Unbalanced and reactive load compensation using an MMCC-based STATCOM with third-harmonic injection. *IEEE Trans Ind Electron* 2019;66(4):2891–902.
- [18] Marzo I, Barrena JA, Sanchez-Ruiz A, Abad G, Muguza I. Reactive power limits of single-phase and three-phase dc-link VSC STATCOMs under negative-sequence voltage and current. In: IECON 2021 – 47th annu. conf. IEEE ind. electron. soc.. 2021, p. 1–8.
- [19] Cupertino AF, Farias JVM, Pereira HA, Seleme SI, Teodorescu R. Comparison of DSCC and SDBC modular multilevel converters for STATCOM application during negative sequence compensation. *IEEE Trans Ind Electron* 2019;66(3):2302–12.
- [20] Luo R, He Y, Liu J. Research on the unbalanced compensation of delta-connected cascaded H-bridge multilevel SVG. *IEEE Trans Ind Electron* 2018;65(11):3439–44.
- [21] Rath IC, Shukla A. A delta connected hybrid STATCOM and dc capacitor voltage balance technique using zero-sequence current. In: PEDES 2020 – 9th IEEE int. conf. power electron. drives energy syst.. 2020.
- [22] Chakraborty S, Mukhopadhyay S, K Biswas S. A hybrid compensator for unbalanced AC distribution system with renewable power. *IEEE Trans Ind Appl* 2022. (early access).
- [23] Yu Y, Konstantinou G, Townsend CD, Aguilera RP, Agelidis VG. Delta-connected cascaded H-bridge multilevel converters for large-scale photovoltaic grid integration. *IEEE Trans Ind Electron* 2017;64(11):8877–86.
- [24] Ouyang S, Liu J, Chen H. Arm current stress reduction technique for a delta-connected solid state transformer using zero-sequence current injection. *IEEE Trans Power Electron* 2021;36(11):12234–50.
- [25] Meligy A, Qoria T, Colak I. Assessment of sequence extraction methods applied to MMC-SDBC STATCOM under distorted grid conditions. *IEEE Trans Power Deliv* 2022. (early access).
- [26] Yang Y, Ma J, Wang S, Wang Z, Jiao N, Liu T, Wu Z. DC-link voltages digital sampling for cascaded H-bridge rectifiers with single voltage sensor under loads unbalanced condition. *IEEE Trans Power Electron* 2023;38(1):7–11.
- [27] He Z, Ma F, Xu Q, Chen Y, Li C, Li M, Guerrero JM, Luo A. Reactive power strategy of cascaded delta-connected STATCOM under asymmetrical voltage conditions. *IEEE J Emerg Sel Top Power Electron* 2017;5(2):784–95.
- [28] Huang H, Zhang L, Oghorada OJ, Mao M. A delta-connected MMCC-based active power conditioner for unbalanced load compensation and harmonic elimination. *Int J Electr Power Energy Syst* 2020;118:105811.
- [29] Jung J-J, Lee J-H, Sul S-K, Son GT, Chung Y-H. DC capacitor voltage balancing control for delta-connected cascaded H-bridge STATCOM considering unbalanced grid and load conditions. *IEEE Trans Power Electron* 2018;33(6):4726–35.
- [30] Zhang J, Wang G, Feng G, Li Y. Analysis of the impact of traction power supply system containing new energy on the power quality of the power system. In: ICPE 2022 – 3rd int. conf. power eng.. Vol. 9, Elsevier Ltd; 2023, p. 363–71.
- [31] Bhonsle DC, Kelkar RB. Analyzing power quality issues in electric arc furnace by modeling. *Energy* 2016;115:830–9.
- [32] Olczykowski Z. Electric arc furnaces as a cause of current and voltage asymmetry. *Energies* 2021;14(16).
- [33] Yuan X, Merk W, Stemmler H, Allmeling J. Stationary-frame generalized integrators for current control of active power filters with zero steady-state error for current harmonics of concern under unbalanced and distorted operating conditions. *IEEE Trans Ind Appl* 2002;38(2):523–32.
- [34] Zmood DN, Holmes DG, Bode GH. Frequency-domain analysis of three-phase linear current regulators. *IEEE Trans Ind Appl* 2001;37(2):601–10.
- [35] Zmood DN, Holmes DG. Stationary frame current regulation of PWM inverters with zero steady-state error. *IEEE Trans Power Electron* 2003;18(3):814–22.
- [36] Bojoi R, Griva G, Bostan V, Guerriero M, Farina F, Profumo F. Current control strategy for power conditioners using sinusoidal signal integrators in synchronous reference frame. *IEEE Trans Power Electron* 2005;20(6):1402–12.
- [37] Limongi LR, Bojoi R, Griva G, Tenconi A. Digital current-control schemes. *IEEE Ind Electron Mag* 2009;3(1):20–31.
- [38] Lascu C, Asiminoaei L, Boldea I, Blaabjerg F. High performance current controller for selective harmonic compensation in active power filters. *IEEE Trans Power Electron* 2007;22(5):1826–35.
- [39] Lascu C, Asiminoaei L, Boldea I, Blaabjerg F. Frequency response analysis of current controllers for selective harmonic compensation in active power filters. *IEEE Trans Ind Electron* 2009;56(2):337–47.
- [40] Yepes AG, Freijedo FD, López Ó, Doval-Gandoy J. High-performance digital resonant controllers implemented with two integrators. *IEEE Trans Power Electron* 2011;26(2):563–76.
- [41] Malinowski M, Gopakumar K, Rodriguez J, Perez MA. A survey on cascaded multilevel inverters. *IEEE Trans Ind Electron* 2010;57(7):2197–206.
- [42] Svensson J, Bongiorno M, Sannino A. Practical implementation of delayed signal cancellation method for phase-sequence separation. *IEEE Trans Power Deliv* 2007;22(1):18–26.
- [43] Etxeberria-Otadui I, Viscarret U, Caballero M, Rufer A, Bacha S. New optimized PWM VSC control structures and strategies under unbalanced voltage transients. *IEEE Trans Ind Electron* 2007;54(5):2902–14.
- [44] Abad G, Sanchez-Ruiz A, Valera-García JJ, Milikua A. Analysis and design guidelines for current control loops of grid-connected converters based on mathematical models. *Energies* 2020;13:1–47.
- [45] Ogata K. Modern control engineering. 5th ed. Pearson; 2010.
- [46] Yepes AG, Freijedo FD, Doval-Gandoy J, Lopez S, Malvar J, Fernandez-Comesana P. Effects of discretization methods on the performance of resonant controllers. *IEEE Trans Power Electron* 2010;25(7):1692–712.
- [47] Vidal A, Freijedo FD, Yepes AG, Malvar J, López Ó, Doval-Gandoy J. Transient response evaluation of stationary-frame resonant current controllers for grid-connected applications. *IET Power Electron* 2014;7(7):1714–24.
- [48] Yepes AG, Freijedo FD, López Ó, Doval-Gandoy J. Analysis and design of resonant current controllers for voltage-source converters by means of nyquist diagrams and sensitivity function. *IEEE Trans Ind Electron* 2011;58(11):5231–50.
- [49] Vidal A, Freijedo FD, Yepes AG, Fernandez-Comesana P, Malvar J, Lopez Ó, Doval-Gandoy J. Assessment and optimization of the transient response of proportional-resonant current controllers for distributed power generation systems. *IEEE Trans Ind Electron* 2013;60(4):1367–83.
- [50] Choi J-W, Sul S-K. Inverter output voltage synthesis using novel dead time compensation. *IEEE Trans Power Electron* 1996;11(2):221–7.
- [51] Muñoz AR, Lipo TA. On-line dead-time compensation technique for open-loop PWM-VSI drives. *IEEE Trans Power Electron* 1999;14(4):683–9.
- [52] Wu CM, Lau W-H, Chung HS-H. Analytical technique for calculating the output harmonics of an H-bridge inverter with dead time. *IEEE Trans Circuits Syst I* 1999;46(5):617–27.
- [53] Yi H, Zhuo F, Wang F. Analysis about overshoot peaks appearing in the current loop with resonant controller. *IEEE J Emerg Sel Top Power Electron* 2016;4(1):26–36.
- [54] Ariffin AE, Munro N. Robust control analysis of a gas-turbine aeroengine. *IEEE Trans Control Syst Technol* 1997;5(2):178–88.